# GST-on-silicon hybrid nanophotonic integrated circuits: a non-volatile quasi-continuously reprogrammable platform

JIAJIU ZHENG,[1] AMEY KHANOLKAR,[2] PEIPENG XU,[1,3] SHANE COLBURN,[1] SANCHIT DESHMUKH,[4] JASON MYERS,[5] JESSE FRANTZ,[5] ERIC POP,[4] JOSHUA HENDRICKSON,[6] JONATHAN DOYLEND,[7] NICHOLAS BOECHLER,[8] AND ARKA MAJUMDAR[1,9,*]

[1]Department of Electrical Engineering, University of Washington, Seattle, WA 98195, USA
[2]Department of Mechanical Engineering, University of Washington, Seattle, WA 98195, USA
[3]Key Laboratory of Photoelectric Materials and Devices of Zhejiang Province, Ningbo University, Ningbo, Zhejiang 315211, China
[4]Department of Electrical Engineering, Stanford University, CA 94305, USA
[5]US Naval Research Lab, Washington, DC 20375, USA
[6]Air Force Research Laboratory, Sensors Directorate, Wright-Patterson Air Force Base, OH 45433, USA
[7]Silicon Photonic Products Division, Intel Corporation, Santa Clara, CA 95054, USA
[8]Department of Mechanical and Aerospace Engineering, University of California, San Diego, La Jolla, CA 92093, USA
[9]Department of Physics, University of Washington, Seattle, WA 98195, USA
*arka@uw.edu

**Abstract:** Reconfiguration of silicon photonic integrated circuits relying on the weak, volatile thermo-optic or electro-optic effect of silicon usually suffers from a large footprint and energy consumption. Here, integrating a phase-change material, $Ge_2Sb_2Te_5$ (GST) with silicon microring resonators, we demonstrate an energy-efficient, compact, non-volatile, reprogrammable platform. By adjusting the energy and number of free-space laser pulses applied to the GST, we characterize the strong broadband attenuation and optical phase modulation effects of the platform, and perform quasi-continuous tuning enabled by thermo-optically-induced phase changes. As a result, a non-volatile optical switch with a high extinction ratio, as large as 33 dB, is demonstrated.

## References and links

1. L. Chrostowski and M. Hochberg, *Silicon Photonics Design: From Devices to Systems* (Cambridge University Press, 2015).
2. M. Hochberg and T. Baehr-Jones, "Towards fabless silicon photonics," Nat. Photonics **4**(8), 492–494 (2010).
3. C. Sun, M. T. Wade, Y. Lee, J. S. Orcutt, L. Alloatti, M. S. Georgas, A. S. Waterman, J. M. Shainline, R. R. Avizienis, S. Lin, B. R. Moss, R. Kumar, F. Pavanello, A. H. Atabaki, H. M. Cook, A. J. Ou, J. C. Leu, Y. H. Chen, K. Asanović, R. J. Ram, M. A. Popović, and V. M. Stojanović, "Single-chip microprocessor that communicates directly using light," Nature **528**(7583), 534–538 (2015).
4. Y. C. Shen, N. C. Harris, S. Skirlo, M. Prabhu, T. Baehr-Jones, M. Hochberg, X. Sun, S. J. Zhao, H. Larochelle, D. Englund, and M. Soljacic, "Deep learning with coherent nanophotonic circuits," Nat. Photonics **11**(7), 441–446 (2017).
5. J. Capmany, I. Gasulla, and D. Perez, "Microwave photonics: The programmable processor," Nat. Photonics **10**(1), 6–8 (2016).
6. P. Dong, W. Qian, H. Liang, R. Shafiiha, N. N. Feng, D. Feng, X. Zheng, A. V. Krishnamoorthy, and M. Asghari, "Low power and compact reconfigurable multiplexing devices based on silicon microring resonators," Opt. Express **18**(10), 9852–9858 (2010).
7. D. Pérez, I. Gasulla, L. Crudgington, D. J. Thomson, A. Z. Khokhar, K. Li, W. Cao, G. Z. Mashanovich, and J. Capmany, "Multipurpose silicon photonics signal processor core," Nat. Commun. **8**(1), 636 (2017).

8.  J. Van Campenhout, W. M. J. Green, S. Assefa, and Y. A. Vlasov, "Low-power, 2 × 2 silicon electro-optic switch with 110-nm bandwidth for broadband reconfigurable optical networks," Opt. Express **17**(26), 24020–24029 (2009).

9.  C. Qiu, X. Ye, R. Soref, L. Yang, and Q. Xu, "Demonstration of reconfigurable electro-optical logic with silicon photonic integrated circuits," Opt. Lett. **37**(19), 3942–3944 (2012).

10.  L. H. Yu, Y. L. Yin, Y. C. Shi, D. X. Dai, and S. L. He, "Thermally tunable silicon photonic microdisk resonator with transparent graphene nanoheaters," Optica **3**(2), 159–166 (2016).

11.  Y. Ikuma, Y. Shoji, M. Kuwahara, X. Wang, K. Kintaka, H. Kawashima, D. Tanaka, and H. Tsuda, "Reversible optical gate switching in Si wire waveguide integrated with $Ge_2Sb_2Te_5$ thin film," Electron. Lett. **46**(21), 1460–1461 (2010).

12.  D. Tanaka, Y. Shoji, M. Kuwahara, X. Wang, K. Kintaka, H. Kawashima, T. Toyosaki, Y. Ikuma, and H. Tsuda, "Ultra-small, self-holding, optical gate switch using $Ge_2Sb_2Te_5$ with a multi-mode Si waveguide," Opt. Express **20**(9), 10283–10294 (2012).

13.  M. Rude, J. Pello, R. E. Simpson, J. Osmond, G. Roelkens, J. J. G. M. van der Tol, and V. Pruneri, "Optical switching at 1.55 μm in silicon racetrack resonators using phase change materials," Appl. Phys. Lett. **103**(14), 141119 (2013).

14.  T. Moriyama, D. Tanaka, P. Jain, H. Kawashima, M. Kuwahara, X. M. Wang, and H. Tsuda, "Ultra-compact, self-holding asymmetric Mach-Zehnder interferometer switch using $Ge_2Sb_2Te_5$ phase-change material," IEICE Electron. Express **11**(15), 20140538 (2014).

15.  M. Stegmaier, C. Rios, H. Bhaskaran, C. D. Wright, and W. H. P. Pernice, "Nonvolatile All-Optical 1 × 2 Switch for Chipscale Photonic Networks," Adv. Opt. Mater. **5**(1), 1600346 (2017).

16.  H. B. Liang, R. Soref, J. W. Mu, A. Majumdar, X. Li, and W. P. Huang, "Simulations of Silicon-on-Insulator Channel-Waveguide Electrooptical 2 × 2 Switches and 1 × 1 Modulators Using a $Ge_2Sb_2Te_5$ Self-Holding Layer," J. Lightwave Technol. **33**(9), 1805–1813 (2015).

17.  Q. Zhang, Y. Zhang, J. Li, R. Soref, T. Gu, and J. Hu, "Broadband nonvolatile photonic switching based on optical phase change materials: beyond the classical figure-of-merit," Opt. Lett. **43**(1), 94–97 (2018).

18.  K. Kato, M. Kuwahara, H. Kawashima, T. Tsuruoka, and H. Tsuda, "Current-driven phase-change optical gate switch using indium-tin-oxide heater," Appl. Phys. Express **10**(7), 072201 (2017).

19.  Z. Yu, J. Zheng, P. Xu, W. Zhang, and Y. Wu, "Ultracompact Electro-Optical Modulator-Based $Ge_2Sb_2Te_5$ on Silicon," IEEE Photonics Technol. Lett. **30**(3), 250–253 (2018).

20.  W. H. P. Pernice and H. Bhaskaran, "Photonic non-volatile memories using phase change materials," Appl. Phys. Lett. **101**(17), 171101 (2012).

21.  C. Rios, P. Hosseini, C. D. Wright, H. Bhaskaran, and W. H. P. Pernice, "On-Chip Photonic Memory Elements Employing Phase-Change Materials," Adv. Mater. **26**(9), 1372–1377 (2014).

22.  C. Rios, M. Stegmaier, P. Hosseini, D. Wang, T. Scherer, C. D. Wright, H. Bhaskaran, and W. H. P. Pernice, "Integrated all-photonic non-volatile multi-level memory," Nat. Photonics **9**(11), 725–732 (2015).

23.  Z. Cheng, C. Ríos, W. H. P. Pernice, C. D. Wright, and H. Bhaskaran, "On-chip photonic synapse," Sci. Adv. **3**(9), e1700160 (2017).

24.  J. Feldmann, M. Stegmaier, N. Gruhler, C. Ríos, H. Bhaskaran, C. D. Wright, and W. H. P. Pernice, "Calculating with light using a chip-scale all-optical abacus," Nat. Commun. **8**(1), 1256 (2017).

25.  F. Xiong, A. D. Liao, D. Estrada, and E. Pop, "Low-Power Switching Of Phase-Change Materials with Carbon Nanotube Electrodes," Science **332**(6029), 568–570 (2011).

26.  M. Wuttig and N. Yamada, "Phase-change materials for rewriteable data storage," Nat. Mater. **6**(11), 824–832 (2007).

27.  K. Shportko, S. Kremers, M. Woda, D. Lencer, J. Robertson, and M. Wuttig, "Resonant bonding in crystalline phase-change materials," Nat. Mater. **7**(8), 653–658 (2008).

28.  M. Wuttig, H. Bhaskaran, and T. Taubner, "Phase-change materials for non-volatile photonic applications," Nat. Photonics **11**(8), 465–476 (2017).

29.  H. S. P. Wong, S. Raoux, S. Kim, J. L. Liang, J. P. Reifenberg, B. Rajendran, M. Asheghi, and K. E. Goodson, "Phase Change Memory," Proc. IEEE **98**(12), 2201–2227 (2010).

30.  S. Raoux and M. Wuttig, *Phase Change Materials: Science and Applications* (Springer, 2009).

31.  D. Loke, T. H. Lee, W. J. Wang, L. P. Shi, R. Zhao, Y. C. Yeo, T. C. Chong, and S. R. Elliott, "Breaking the Speed Limits of Phase-Change Memory," Science **336**(6088), 1566–1569 (2012).

32.  S. Raoux, F. Xiong, M. Wuttig, and E. Pop, "Phase change materials and phase change memory," MRS Bull. **39**(8), 703–710 (2014).

33.  S. Raoux, G. W. Burr, M. J. Breitwisch, C. T. Rettner, Y. C. Chen, R. M. Shelby, M. Salinga, D. Krebs, S. H. Chen, H. L. Lung, and C. H. Lam, "Phase-change random access memory: A scalable technology," IBM J. Res. Develop. **52**(4–5), 465–479 (2008).

34.  Y. Wang, X. Wang, J. Flueckiger, H. Yun, W. Shi, R. Bojko, N. A. F. Jaeger, and L. Chrostowski, "Focusing sub-wavelength grating couplers with low back reflections for rapid prototyping of silicon photonic circuits," Opt. Express **22**(17), 20652–20662 (2014).

35.  M. Stegmaier, C. Rios, H. Bhaskaran, and W. H. P. Pernice, "Thermo-optical Effect in Phase-Change Nanophotonics," ACS Photonics **3**(5), 828–835 (2016).

36.  V. R. Almeida and M. Lipson, "Optical bistability on a silicon chip," Opt. Lett. **29**(20), 2387–2389 (2004).

37. Y. K. Wu, K. Liu, D. W. Li, Y. N. Guo, and S. Pan, "In situ AFM and Raman spectroscopy study of the crystallization behavior of $Ge_2Sb_2Te_5$ films at different temperature," Appl. Surf. Sci. **258**(4), 1619–1623 (2011).
38. G. H. Wei, T. K. Stanev, D. A. Czaplewski, I. W. Jung, and N. P. Stern, "Silicon-nitride photonic circuits interfaced with monolayer $MoS_2$," Appl. Phys. Lett. **107**(9), 091112 (2015).
39. W. Bogaerts, P. De Heyn, T. Van Vaerenbergh, K. De Vos, S. K. Selvaraja, T. Claes, P. Dumon, P. Bienstman, D. Van Thourhout, and R. Baets, "Silicon microring resonators," Laser Photonics Rev. **6**(1), 47–73 (2012).
40. C. D. Wright, Y. Liu, K. I. Kohary, M. M. Aziz, and R. J. Hicken, "Arithmetic and Biologically-Inspired Computing Using Phase-Change Materials," Adv. Mater. **23**(30), 3408–3413 (2011).

## 1. Introduction

Silicon photonics has been extensively studied in the past decade for many applications including optical interconnects, sensing, and signal processing [1], due to its potential to realize high component density and reduced power consumption, and its compatibility with complementary metal-oxide-semiconductor (CMOS) fabrication technology. With silicon photonics going fabless [2], large-scale silicon photonic integrated circuits (PICs) have recently become a reality [3,4]. Many of these PICs feature system reconfigurability to benefit from the cost-effective mass manufacturing of a universal platform instead of task-specific customized circuits [5]. This is analogous to the benefit of an electronic field-programmable gate array (FPGA) over an application specific integrated circuit (ASIC). Current reconfigurable silicon PICs, however, primarily rely on the thermo-optic [4,6,7] or electro-optic [8,9] effect of silicon, and thus suffer from several limitations. Both effects produce minimal tuning of the refractive index (usually $\Delta n < 0.01$), leading to devices with large footprint (at least few tens of microns for the length of active regions) and energy consumption (typically several milliwatts) [10]. The volatile nature of these effects also necessitates a constant supply of the electric power.

Recently, phase-change materials (PCMs) have shown great promise for non-volatile integrated photonic applications such as optical switches [11–18], optical modulators [16,19], photonic memories [20–22], and optical computing [23,24]. By applying short optical or electrical pulses with very low energy (as low as femtojoules) [22,25], PCMs can be reversibly switched between the covalent-bonded amorphous phase and the resonant-bonded crystalline phase. These two phases exhibit dramatically high contrast in the electrical resistivity and optical constants ($\Delta n > 1$) over a broad wavelength range from the visible to infrared (IR) spectral region [26–28]. Additionally, by carefully controlling the excitation signal, intermediate states between the two phases can be reached, resulting in multi-level operation [22–24,29]. The transition between the two phases takes place on a picosecond to sub-nanosecond timescale for amorphization [30], and on a sub-nanosecond to nanosecond timescale for crystallization [30,31], enabling ultra-fast operation for potentially over $10^{15}$ switching cycles [32]. The switched final state can also remain intact for several years under ambient conditions without any external power [26,29]. Moreover, PCMs are extremely scalable and can be shrunk to the nanoscale [33]. Therefore, PCM-integrated silicon photonics presents a promising solution to energy-efficient, ultra-compact [14,19], and ultra-fast non-volatile reprogrammable PICs. While several devices based on the GST-SOI platform have already been reported [12–14], none of them have taken into account the pulse energy- or number-dependent optical response that has provided access to a desirable multi-level memory in silicon nitride photonics [22]. Also, the fundamental properties of this platform, such as attenuation and optical phase modulation, have not yet been systematically explored.

In this work, utilizing $Ge_2Sb_2Te_5$ (GST), one of the most well-known PCMs, we build a non-volatile, quasi-continuously reprogrammable, GST-on-silicon hybrid nanophotonic integrated platform based on microring resonators. We successfully characterize both the strong broadband attenuation and optical phase modulation properties of the GST-on-silicon platform. By controlling the pulse energy and number of pulses applied to the GST from a pulsed laser, we demonstrate quasi-continuous tuning of the GST state, and the subsequent tuning of the attenuation and resonance of microring resonators. Designed to achieve near

critical coupling when the GST is in the amorphous state, the microring resonators show a very high extinction ratio of optical switching (up to 33 dB) between the amorphous and crystalline states.

## 2. Structure and fabrication

As illustrated in Fig. 1(a), our GST-on-silicon platform integrates GST with silicon ridge waveguides where light is evanescently coupled with the GST. Due to the dramatic difference in the complex refractive index between amorphous GST (aGST) and crystalline GST (cGST), the light mode and complex effective index $n_{eff}$ of the hybrid waveguide will be strongly modified once GST is switched between two phases, as is shown in Figs. 1(b) and 1(c). The simulations are performed using the frequency-domain finite-element method (FEM). The transmission and phase properties of silicon PICs using such a structure can thus be significantly altered.
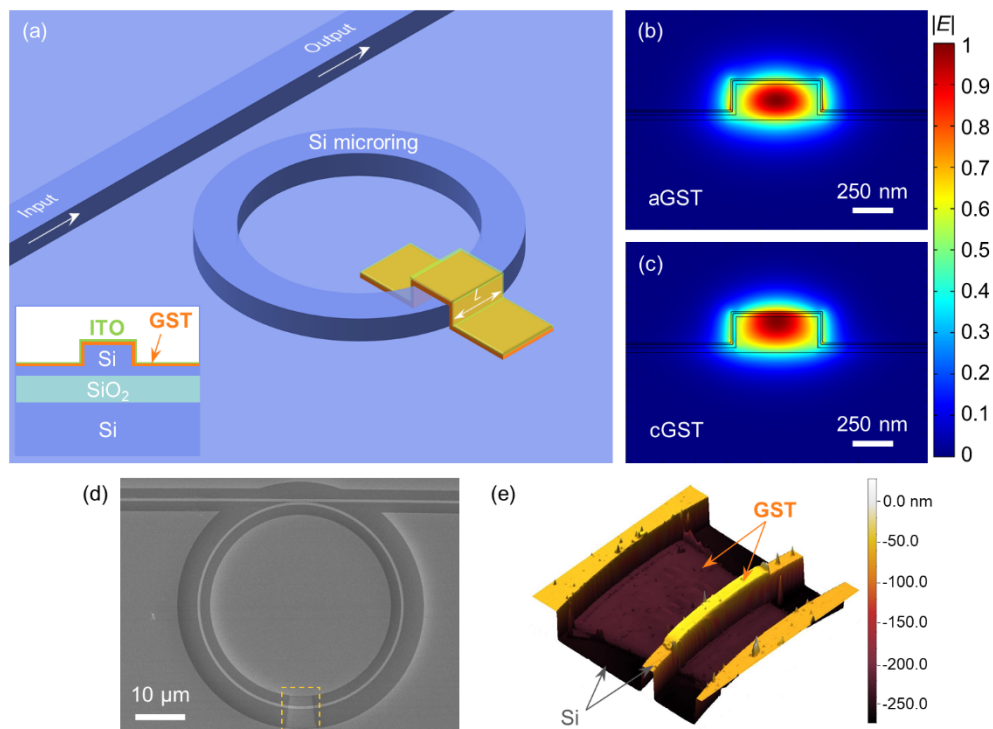


Fig. 1. GST-on-silicon hybrid nanophotonic integrated circuits (nano-PICs). (a) Schematic of the platform. Inset: cross-section of the hybrid waveguide. To emphasize the gap between the waveguide and the ring, the schematic is not in scale. (b), (c) Fundamental quasi-transversal electric (TE) mode profiles (normalized amplitude profiles of the electric field) of the hybrid waveguide at 1550 nm for (b) aGST with $n_{eff} = 2.62 - 0.0024i$ and (c) cGST with $n_{eff} = 2.97 - 0.22i$. Both were simulated with frequency-domain FEM using the optical constants of GST and ITO measured by ellipsometry. (d) SEM of a microring with 5 μm as-deposited GST. (e) AFM height map of the region highlighted by the yellow dashed rectangle in (d).

We fabricated the hybrid platform on a silicon-on-insulator (SOI) wafer with a 220-nm-thick silicon layer on top of a 3-μm-thick buried oxide layer. The pattern, including the 500-nm-wide waveguides, microring resonators, and grating couplers [34], was defined by a JEOL JBX-6300FS 100kV electron-beam lithography (EBL) system using positive tone ZEP-520A resist. After development, 190 nm partially etched ridge waveguides were made by an inductively coupled plasma reactive ion etching (ICP-RIE) process. The partially etched design is chosen to reduce the step height for the GST deposition later in the process and to

enhance the coupling between bus waveguides and microrings. The enhanced coupling maintains the critical coupling condition (where the round-trip loss rate is the same as the coupling rate) in the microring resonator, in the presence of high loss from the GST. The devices were then measured to obtain the reference transmission spectra. A second EBL exposure using positive tone poly(methyl methacrylate) (PMMA) resist was subsequently carried out to create windows for the GST deposition. After development, 20 nm of GST was sputtered onto the chip from a GST target (AJA International) using a magnetron sputtering system, and then capped with 11 nm of indium tin oxide (ITO) to protect the GST from oxidation. The deposited ITO layer here is relatively transparent over the visible and near-IR spectral region according to ellipsometry measurements (extinction coefficient $\kappa < 0.002$ from 480 nm to 1700 nm, and much smaller than that of GST in the amorphous and crystalline state). Finally, the lift-off of the GST/ITO layers was completed using methylene chloride. Figure 1(d) shows a scanning electron micrograph (SEM) of one of the fabricated microring resonators partially covered with an as-deposited GST strip (length $L = 5$ μm). Using atomic force microscopy (AFM), as is shown in Fig. 1(e), we confirmed a 31-nm-thick smooth thin film of GST/ITO was deposited on the silicon waveguide with an average root mean square (RMS) surface roughness of 2.2 nm (which is much shorter than the wavelength of interest).
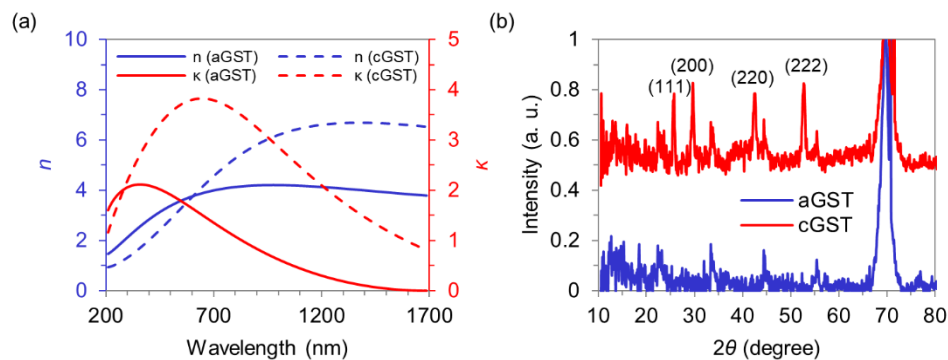


Fig. 2. GST characterization. (a) complex refractive index of aGST and cGST as a function of wavelength. (b) XRD data of aGST and cGST. The curve of cGST is offset vertically for clarity.

## 3. Results and discussion

To characterize the properties of the GST-on-silicon platform, we measured the transmission spectrum of 40 microring resonators (20 μm radius, and a gap of 100 nm between the bus waveguide and the microring) covered with various lengths of GST using a vertical fiber-coupling setup. Focusing sub-wavelength grating couplers [34] were utilized to couple light from a tunable continuous wave laser (Santec TSL-510) to the waveguides and collect light on the other side of the waveguides into a low-noise power meter (Keysight 81634B) via single-mode fibers (SMFs). The power of the coupled light was selected to be low enough (< 100 μW) to prevent any phase transition of the GST and minimize the thermal-optic effects of the GST [35] and silicon [36]. The polarization of the input light was controlled to match the fundamental quasi-TE mode of the waveguide by a manual fiber polarization controller (Thorlabs FPC526). The temperature of the test stage was fixed at 20°C using a thermoelectric controller (TEC, TE Technology TC-720), so as to avoid any thermal shift of the resonators. For each device, we performed the transmission measurement: (i) before the GST deposition to record the intrinsic loss and resonant wavelength of each microring, (ii) right after the GST deposition (which is aGST), and then (iii) after rapid thermal annealing (RTA) of the chip at 200 °C for 10 mins in a $N_2$ atmosphere to change the GST from the amorphous to the crystalline state. We verified the states by ellipsometry and X-ray diffraction (XRD) measurement of a blanket GST layer deposited on a silicon wafer. As

shown in Fig. 2(a), the extracted optical constants have high contrast over a broad spectral region between as-deposited and annealed GST and agree well with previously measured values from aGST and cGST, respectively [27,28]. The XRD data in Fig. 2(b) show that the XRD distribution changed from a disordered aGST pattern to a typical diffraction pattern of fcc cGST after RTA with four characteristic peaks [37]. The strong signal near 70° in Fig. 2(b) is from the silicon substrate, which covers the (420) peak of cGST.

Figure 3(a) shows the representative output spectra of microrings in the amorphous and crystalline states, which are strongly related to the state and the length of the GST. Two spectra, corresponding to aGST and cGST, for each length of GST are plotted on the same scale, where each set corresponding to a different length is vertically offset for clarity. In both states, with an increase of the GST length $L$ (shown on the right axis of the plot), the linewidths of the resonant dips broaden, corresponding to the increase in loss, and a red-shift of the spectrum is observed, corresponding to the increase in the effective index. Similar broadening and red-shift of the resonances can be observed for every microring upon switching the GST from the amorphous to the crystalline state. The absorptive and refractive modulation effects introduced by the GST are so substantial that we observe a distinct color change between aGST and cGST under a microscope, as is shown in Figs. 3(b) and 3(c). We note that with increasing length of the GST, the round-trip loss rate increases, while the coupling rate between the waveguide and the ring remains the same. Hence, the ring resonator goes from being over-coupled, to critically-coupled, then under-coupled. This can be observed from Fig. 3(a), where the transmission dip changes depending on the length of aGST.
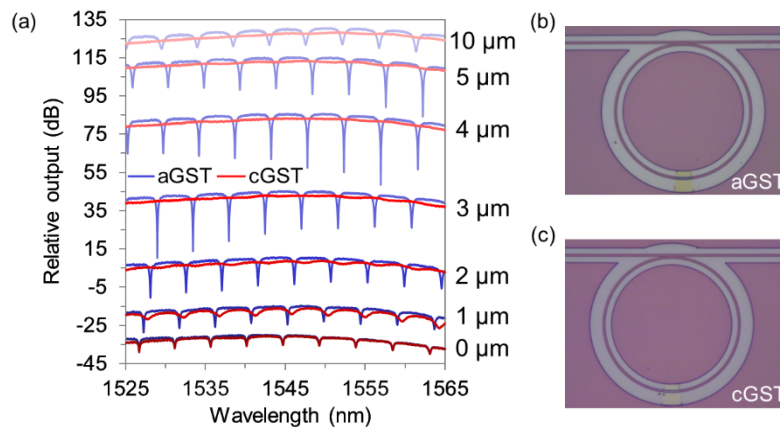


Fig. 3. Transmission measurement of the microrings with GST. (a) Representative output spectra of microrings with different lengths of GST, in both the amorphous and crystalline states. For each length of GST, the cGST and aGST spectra are in scale, while each set of spectra for a different length of GST is offset vertically for clarity. (b), (c) Microscope images of a microring with 5 μm (b) aGST and (c) cGST.

To quantitatively describe the modulation effects, we extracted the quality factor $Q$ and resonant wavelength of each dip by fitting the measured resonances to the Lorentzian lineshape function [Fig. 4(a)]. We could not fit the data of the microrings with cGST of length $L > 2$ μm since the visibility of the resonance is significantly reduced due to strong attenuation from the cGST, as is shown in Fig. 3(a). As the quality factor and the free spectral range (FSR) of the bare silicon microring (without any GST) remain unchanged throughout the fabrication process [shown by the curves denoted as "0 μm" GST in Fig. 3(a)], we assume that the intrinsic loss (composed of scattering loss, material absorption loss, and bending loss) of the microrings remains unchanged after the GST deposition and RTA. The loss introduced by GST can then be estimated as the difference in the loss of the microring before and after GST deposition [38]:

$$\text{Loss} = \alpha L + \alpha_0 \approx 2\pi R \cdot \frac{2\pi n_g}{\lambda_0} \cdot \left(\frac{1}{Q} - \frac{1}{Q_0}\right) = \frac{2\pi \lambda_0}{\text{FSR}} \cdot \left(\frac{1}{Q} - \frac{1}{Q_0}\right), \tag{1}$$

where $\alpha$ is the attenuation coefficient of the GST-on-silicon hybrid waveguide, $\alpha_0$ is the mode mismatch loss between the regular silicon waveguide and the hybrid waveguide, $R = 20$ μm is the radius of the microrings, $\lambda_0$ is the resonant wavelength, $Q_0$ and $Q$ are the quality factors of the same microring before and after the GST deposition, FSR is the free spectral range of the microring, and $n_g = \lambda_0^2/(\text{FSR} \cdot 2\pi R)$ is the group index averaged over the whole ring with partial GST coverage. Here, the change in FSR and $n_g$ due to the GST deposition is neglected because of the limited coverage area of GST on the microrings. As plotted in Fig. 4(b), the GST-introduced loss is linearly proportional to the length of the GST. From this, we obtained the attenuation coefficient of the hybrid waveguide near 1550 nm to be $\alpha_{aGST} = 0.27 \pm 0.04$ dB/μm for aGST and $\alpha_{cGST} = 7.6 \pm 1.0$ dB/μm for cGST. The uncertainty noted is obtained from the upper and lower limit of the confidence interval (95%) for estimated parameters by linear regression analysis. Therefore, the attenuation modulation effect from aGST to cGST is around 7.3 dB/μm. Compared with the simulation results, the experimental attenuation coefficient for cGST agrees quite well with the theoretical value of 7.7 dB/μm, whereas that for aGST is much larger than the expected 0.08 dB/μm. We attribute this inconsistency to the unwanted scattering loss due to the surface roughness of GST. The scattering loss is negligible when the device is in the lossy crystalline state. However, the scattering loss becomes dominant when the absorption rate of GST is relatively small in the amorphous state. The extracted mode mismatch loss is less than 0.5 dB in both states and is ignored in calculating the attenuation coefficient using Eq. (1), except in the amorphous state.
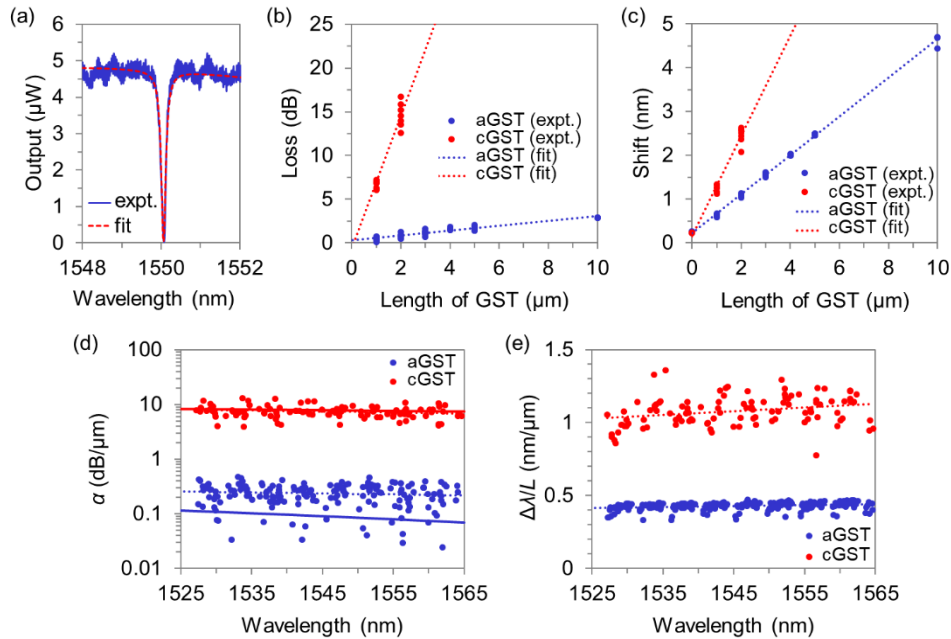


Fig. 4. Characterization of the GST-on-silicon platform using microring resonators. (a) Lorentzian fitting of the spectrum for the resonant dips in a ring with $Q \sim 11,000$ near 1550 nm. (b), (c) GST length dependent (b) loss and (c) spectral shift of the microrings for aGST and cGST with respect to those of the intrinsic microrings. Every dot represents a single device. (d), (e) Wavelength dependent (d) attenuation coefficient and (e) resonance shift per unit GST length for aGST and cGST with respect to the reference (before GST deposition) (dots: experiment data, dotted lines: linear fitting, solid lines: simulation).

The linear increase of the red spectral shift $\Delta\lambda$ with respect to the reference (before GST deposition) as a function of the GST length is shown in Fig. 4(c). We fit the resonance shifts per unit GST length $\Delta\lambda/L$ near 1550 nm to be $0.444 \pm 0.007$ nm/μm and $1.14 \pm 0.12$ nm/μm for aGST and cGST, respectively. Thus, the optical phase modulation effect from aGST to cGST is around 0.70 nm/μm. We observe that there is a residual shift of ~0.2 nm for every microring after the GST deposition, as is reflected by the non-zero shift at $L = 0$ μm. We attribute this to an irreversible modification of the ring resonators during the deposition process, possibly from residual resist left over from the lift-off process. The spectral shift can also be theoretically estimated [39] by

$$\frac{\Delta\lambda}{L} \approx \frac{\Delta n_{\text{eff}} \lambda_0}{2\pi R n_{\text{eff0}}},$$ (2)

where $n_{\text{eff0}}$ is the real part of the effective index for the bare silicon waveguide, and $\Delta n_{\text{eff}}$ is the real part of effective index change. The effective index $n_{\text{eff0}}$ is used instead of group index $n_g$ because only a small portion of the ring resonator is modified, unlike the case described in [39]. According to the simulated waveguide modes, $\Delta\lambda/L$ is 0.98 nm/μm and 2.76 nm/μm for aGST and cGST, respectively. Potential causes for the discrepancy between the theory and experiment are: the modification of the GST refractive index upon shrinking the GST from the wafer size into a small scale, or a non-conformal coverage of GST due to the directionality of sputtering. From the experimental data, we estimate the refractive indices of the nano-patterned GST to be $n_{\text{aGST}} \approx 2.58 - 0.12i$ and $n_{\text{cGST}} \approx 4.68 - 1.92i$, whereas the pristine GST indices are (measured by ellipsometry) $n_{\text{aGST}} = 3.89 - 0.02i$ and $n_{\text{cGST}} = 6.63 - 1.09i$. The increased imaginary value for aGST is, however, primarily due to the extra scattering loss. Measurement of refractive indices of nano-patterned GST is generally difficult and our results indicate that high $Q$-resonators can potentially be used to characterize properties of materials on the nanoscale. Figures 4(d) and 4(e) summarize the extracted attenuation coefficient and the resonance shift per unit GST length, as a function of the wavelength. Both the attenuation coefficient and the resonance shift exhibit broadband behavior over the whole C band (1530 nm-1565 nm) for both aGST and cGST, as was expected from the simulations. Notably, a close match was observed between the simulation line and the linear fitting line of experimental data for the attenuation coefficient of cGST.
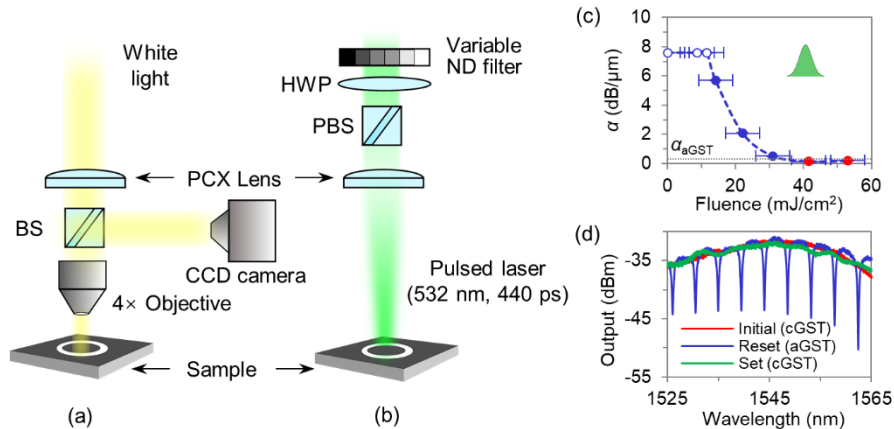


Fig. 5. Determination of GST phase transition conditions by an optical heating setup. (a) Schematic of the optical imaging system (PCX Lens: plano-convex lens). (b) Schematic of the optical pumping system. (c) Induced attenuation coefficient as a function of the fluence of a single laser pulse (white, blue, and red dots denote devices that retained the crystalline state, had intermediate states of GST, and had damaged GST, respectively). Inset: the green Gaussian pulse denotes that only a single pulse was used for this experiment. (d) Sample output spectra of a microring with 4 μm GST in the determined set and reset conditions.

The state of GST can be reversibly programmed by the application of heat via optical or electrical pulses. Here, we explore reversible and quasi-continuous tuning of the GST by a 532-nm actively $Q$-switched pulsed diode-pumped solid-state (DPSS) laser (Coherent HELIOS 532-3-50) with 440 ps pulse duration. As illustrated in Fig. 5(a), an optical imaging system was used to locate the devices of interest under white light. Once the CCD camera, the beam splitter (BS), and the objective were moved away to avoid laser damage, the setup became an optical pumping system [Fig. 5(b)] enabling the pulsed laser to switch the GST. The pump energy of the optical pulses was adjusted by a variable neutral-density (ND) filter and a half-wave plate (HWP), along with a polarizing beam splitter (PBS). Rotating the HWP in the beam path rotated the polarization of the pump laser, the vertical component of which was transmitted to the sample by after passing through the PBS. The pump energy was measured by a laser power meter (Coherent FieldMaxII-TO) with a thermopile sensor (Coherent PM10). The number and repetition rate of the pulses were controlled by providing a TTL signal to the $Q$-switch of the laser using a dual channel arbitrary function generator (Tektronix AFG3022B). In order to align the laser beam spot (diameter ~120 μm) with the GST strip, we used the pump laser to burn a hole on the edge of the chip with consecutive high-energy pulses, marked the contour of the hole on the screen of the imaging system, and then moved the target GST strip to the center of the mark with a 3-axis stage. After optically heating the sample, the chip was taken back to the fiber setup for transmission measurement.

To realize quasi-continuous tuning of the hybrid platform, we first determined the set (crystallization) and the reset (amorphization) condition of the GST. For amorphization, the GST should be melted and then rapidly quenched to maintain its disordered state by a single short pulse. In contrast, heating the GST to just above its crystallization temperature, but below the melting point, by a long-enough sequence of short pulses or a single long pulse, converts the lattice arrangement to a crystalline or partially crystalline state. We chose several microrings with the same length ($L = 5$ μm) of fully crystalline GST (after RTA) and illuminated the GST with a single pulse of different energies (a different pulse energy for each ring). The attenuation coefficient introduced by the GST was then extracted from the transmission spectrum. Because the attenuation coefficient reflects the state of GST or the degree of crystallization, the pulse that leads the attenuation coefficient to drop to around the previously fitted value of $\alpha_{aGST}$ can serve as the reset pulse. Similarly, the pulse of lower energy that maintained the initial crystalline GST attenuation coefficient $\alpha_{cGST}$ can be identified as an appropriate set pulse. As is shown in Fig. 5(c), with the increase of the laser fluence, the attenuation coefficient decreases from $\alpha_{cGST}$ to a value below $\alpha_{aGST}$ (red dots in the figure), corresponding to damage to the GST, which was verified by microscope inspection. We estimate the error in our power measurements to be ~10 mJ/cm$^2$. Such a large error is primarily due to the free-space setup and can be potentially reduced by guiding the light on-chip. We chose the single reset pulse fluence to be ~31 mJ/cm$^2$ which was below the damage fluence, and each of the set pulses to be ~10 mJ/cm$^2$. To fully crystallize the GST, we applied 450 consecutive set pulses with a repetition rate of 50 kHz to accumulate heat. These thermal conditions are comparable to those used previously [40] and justified by conducting the reset and set pulses back and forth several times on the same microring and comparing the attenuation coefficient to the fitted values. Figure 5(d) shows the typical spectra of one microring with 4 μm GST after the set and reset pulses. The single reset pulse reduced the attenuation coefficient to 0.62 dB/μm, while the set sequence successfully made the spectrum recover back to the initial state (cGST). Considering the effective area of the GST used in the hybrid waveguides, the equivalent energies of each pulse to switch the GST to amorphous and crystalline state are only ~620 pJ (~9 aJ/nm$^3$) and ~200 pJ (~3 aJ/nm$^3$), respectively, which are comparable to previous reports with similar volumes of GST [13,22]. We note that the energy-efficiency of our device is only an order of magnitude larger than the fundamental limit, estimated to be ~1.2 aJ/nm$^3$ [32]. We emphasize that as the phase transition is non-volatile, no more energy is needed after the switching process. It is due to this non-volatile

nature of GST phase change where the PCM-based tuning mechanisms out-perform traditional thermo-optic or electro-optic mechanisms in terms of total energy-efficiency for reconfigurable photonics.

The set and reset pulses allow us to control the hybrid nano-PICs in a quasi-continuous manner. As is shown in Fig. 6, a microring with 2 μm of fully crystalline GST was pumped by a reset pulse to convert the GST to the amorphous state. Since the loss of the microring for aGST is close to the transmission loss in the coupling region, the critical coupling condition was reached in the amorphous state, enabling deep dips in the transmission spectrum [Figs. 6(a) and 6(b)]. To achieve intermediate states, we exploited the heat accumulation effect by applying a succession of excitations, each comprised of 25 set pulses to the GST on the microring. With the increase of the number of excitations, the resonance linewidths increased, the depth of the resonances diminished, and the resonances shifted to longer wavelengths, implying an increased fraction of crystallization in the GST. With five 25 set pulse excitations, the spectrum of the microring is almost identical to that where the GST is in the fully crystalline state. Due to the remarkable absorptive and refractive modulation effects of GST, the transmission of the microring at 1551.5 nm shows a switching effect with an extinction ratio of 33 dB [Fig. 6(b)]. To justify the crystallization procedure, we extracted the attenuation coefficient of the hybrid waveguide at around 1551.5 nm, as is shown in Fig. 6(c). The attenuation coefficient gradually increased to ~7 dB/μm, which is close to the previously fitted value $\alpha_{cGST}$. We repeated this experiment with several other rings, and observed similar qualitative behavior, although quantitative match was not obtained. We attribute this uncertainty to the small shifts in the relative position between the laser beam spot and the GST strip. Note that, although we achieved each intermediate state from its last state in one direction, our experiment implies that we can achieve any pre-defined intermediate states from fully crystalline GST by first applying a reset pulse and then applying a variable number of set pulses. Although packets of 25 pulses were used in our experiment, we note that reducing the number of set pulses in each excitation, more intermediate states can be realized.
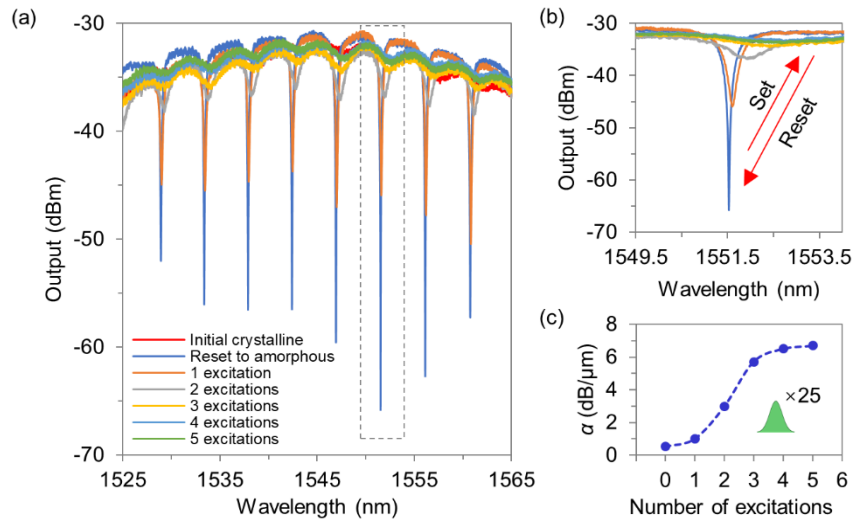


Fig. 6. Quasi-continuous tuning of the GST-on-silicon hybrid nano-PICs. (a) Output spectra of a microring with 2 μm GST under different number of excitations, where "excitation" denotes a packet of 25 consecutive pulses applied at 50 kHz repetition rate. (b) A zoom-in inspection of the region highlighted by the grey dashed rectangle in the spectra in (a). (c) Attenuation coefficient of the hybrid waveguide as a function of the number of excitations. Inset: the green Gaussian pulse with "×25" denote the excitation process.

## 4. Summary

We have characterized the broadband attenuation and optical phase modulation effects of the GST-on-silicon hybrid nano-PICs using microring resonators. With different pulse energy and number of laser pulses, it was shown that the GST on the hybrid platform can be reversibly switched between amorphous and crystalline states and quasi-continuously tuned to several intermediate states. Based on this platform, a non-volatile optical switch with a high extinction ratio up to 33 dB was demonstrated. Our research is only a first step towards future large-scale reprogrammable silicon PICs. For instance, with appropriate design, a broadband low-loss $2 \times 2$ optical switch [17] could be realized, which would be the building block for a future non-volatile routing network and optical FPGA. It is worth noting that the free-space optical heating setup used in this work is not a scalable method for complex PICs due to the slow locating process. While on-chip optical heating can help modulate the device fast and accurately, the complexity of the PICs may still be limited because of the difficulties in routing the light and high loss from the PCM [24]. To flexibly control the phase transition, local electrical heating either using another transparent conductive material or silicon itself may be preferable [18,19], wherein mature CMOS electronics can be leveraged to make reprogrammable photonic-electronic integrated circuits.